LAWRENCE
LIVERMORE
NATIONAL
LABORATORY

LLNL-JRNL-467883

The orientation and morphology of Pt precipitates within sapphire

M. K. Santala, V. R. Radmilovic, R. Giulian, M. C. Ridgway, R. Gronsky, A. M. Glaeser

January 27, 2011

Acta Materialia

Disclaimer

Accepted by Acta Materialia *April 2011*

The orientation and morphology of Pt precipitates in sapphire

Melissa K. Santala[1], Velimir Radmilovic[2,3], Raquel Giulian[4], Mark C. Ridgway[4], Ronald Gronsky[5] and Andreas M. Glaeser[5]

[1]Condensed Matter and Materials Division, Lawrence Livermore National Laboratory, Livermore, CA, USA
[2]National Center for Electron Microscopy, Lawrence Berkeley National Laboratory, Berkeley, CA, USA
[3]Nanotechnology and Functional Materials Center, Faculty of Technology and Metallurgy, University of Belgrade, Serbia
[4]Department of Electronic Materials Engineering, Australian National University, Canberra, ACT, Australia
[5]Department of Materials Science and Engineering, University of California, Berkeley, CA, USA

Abstract

The orientation relationship, crystallography and structure of heterointerfaces influence their energy, and collectively these interface properties can exert a profound effect on a wide range of multiphase-material properties. In this study, stable interfaces were identified and relative interfacial energies were determined in a model oxide-metal system from measurements of the shapes of Pt inclusions in a sapphire matrix. Platinum precipitates were formed in sapphire via ion implantation followed by thermal annealing in air. The morphology of precipitates with a high-symmetry orientation relationship was determined after annealing at 1600°C for 100 h, processing conditions anticipated to result in equilibrium morphology if shape changes are only diffusion limited. The precipitates were found to have both faceted and rough interfaces. The facets coincided with low-index planes of sapphire. All sapphire facets that appear in the Wulff shape of undoped sapphire at 1600°C were observed, but additional facets also appeared. Lack of complete convergence on an equilibrium shape is believed to be due to the absence of ledge-producing defects in some particles, and the inability to overcome the nucleation energy barriers required to form ledges.

1. Introduction

Many technologies and devices rely upon interfaces between a metal and an oxide ceramic. The microstructures, properties, and lifetimes of multimaterial structures can be affected by the structure, energy, and stability of these interfaces. Despite their profound impact on materials and device properties, many fundamental properties of ceramic-metal interfaces are not well understood. This is in part due to the chemical and crystallographic complexity and variety encompassed by heterointerfaces. For this reason, experimental and theoretical studies of the structure, energy, and properties of ceramic-metal interfaces are important in materials science and related technological fields [1-5].

Interfacial energy is of general interest, because it is a fundamental thermodynamic property of interfaces. The ceramic-metal interfacial energy affects the contact angle, work of adhesion, and mechanical strength of the interface and has special significance for systems processed by routes involving a liquid phase, such as liquid-metal infiltration [6], or by soldering or brazing [7-11]. Sessile-drop experiments, [7, 8, 12-15] in which the shape of a liquid-metal droplet on a ceramic substrate is characterized, have been used to assess the contact angle. Similarly, the equilibrium shapes of solid-metal particles on planar ceramic substrates can be used to deduce the ceramic-metal interfacial energy and the work of adhesion [16], and can provide information on the relative energies of the metal surfaces [17].

Well-defined planar interfaces can be produced by thin-film deposition or by solid-state diffusion bonding. Interfaces formed by deposition or diffusion bonding are generally not in equilibrium and have limited utility in the study of interface thermodynamics, but they provide a convenient platform for studies of mechanical properties [18-25], crystallographic interfacial relationships [4, 26, 27], and chemical bonding [5, 27-31]. In polycrystalline materials, grain-boundary grooving behavior can be used to assess interfacial energies, mechanisms of diffusion near the interfaces, and rate-controlling diffusivities [32, 33].

Despite their many attractive features, experiments on planar interfaces limit the ability to assess the anisotropy of the interfacial energy. As has been demonstrated for ceramic-vapor [34-37], metal-vapor [17, 38, 39], liquid-metal–solid-metal [40] and liquid-metal–ceramic interfaces [41],

anisotropy, even when small, can have a significant effect on the rate and nature of morphological evolution, with facets playing a pivotal role. One method of studying interfacial-energy anisotropy is to examine embedded phases, as in this study. Under the proper experimental conditions, the quantitative assessment of morphology may be used to extract information about the stability and relative interfacial energies of different interfaces, as done in the Cu-MgO system [42, 43].

In this study, Pt precipitates were formed in sapphire (single crystal α-Al_2O_3) via ion implantation followed by thermal annealing in air. Alumina (Al_2O_3) was chosen for this model study, because it is one of the most widely used and studied ceramics. Elemental Pt was chosen as the metallic component for some of the same reasons it is used to bond Al_2O_3 in high-temperature and corrosive environments and for applications subject to repeated thermal cycling: its coefficient of thermal expansion (CTE) [44-47] and melting temperature are similar to sapphire, and it can form a strong bond with Al_2O_3 [18-21, 48]. Thus Pt embedded in sapphire is chemically and mechanically stable over a broad range of processing conditions. Based on the CTEs, if Pt precipitates in sapphire are quenched to room temperature from just below the melting temperature of Pt, the resulting linear strain is <0.7%, on average. While this is a considerable thermal-expansion mismatch, of all elemental metals, Pt provides one of the best matches to α-Al_2O_3, and, unlike other metals with a similar CTE, such as Nb, Pt is resistant to oxidation. The high melting temperature of Pt permits annealing at temperatures where diffusion in the sapphire is rapid enough to allow morphological equilibration of solid Pt precipitates to occur in experimentally accessible times. The experiments here were conducted to determine the morphology of equilibrated (or nearly equilibrated) Pt precipitates in sapphire which developed with the orientation relationship $\mathbf{c}(0001)_\alpha||(111)_{Pt}$; $[10\bar{1}0]_\alpha||[1\bar{1}0]_{Pt}$. The experimental results identify energetically favorable morphologies, from which one can draw conclusions about the crystallographic dependence of interfacial-energy anisotropy in this model ceramic-metal system.

2. Background

The morphology of precipitates and inclusions can affect mechanical, optical, and other properties of composites. The precipitate-matrix orientation relationship (OR) and the precipitate shape and size can all affect the crystallography, structure, and energy of the interfaces. Misfit can

cause strains in both the precipitate and the matrix, and the elastic-misfit energy affects the equilibrium state of the system. The interaction between the precipitate and matrix is affected by the OR, the elastic anisotropy of the precipitate and matrix, and the precipitate shape and size. The interfacial-energy and elastic-misfit-energy contributions scale differently with particle size, and thus, when both contributions are present, the equilibrium shape represents a size-dependent minimization of their sum. When elastic-energy contributions are negligible, a size-independent equilibrium shape results. The nature of the shape, particularly the presence of facets, and the precipitate size can affect the ability of the system to reach this equilibrium shape in an accessible timeframe. We review some of the key issues that affect our interpretation of the experimental results obtained in this study.

2.1 *Equilibrium morphologies of crystals and crystalline inclusions*

For a strain-free centro-symmetric crystal in an isotropic medium, Wulff defined the relationship between the surface energy and the equilibrium crystal morphology [49] that minimizes the total surface energy of a crystal of fixed volume. The Wulff theorem states that for all surfaces that are part of the equilibrium (Wulff) shape, the ratio of the specific surface energy of a surface of orientation j, γ_j, to the separation distance, l_j, between parallel surfaces of this orientation measured along a surface normal is a constant, *i.e.*,

$$\gamma_j / l_j = \text{constant}. \quad (1)$$

Thus, measurements of the relative particle dimensions of a crystal in morphological equilibrium may be used to determine the relative energies of the crystallographically distinct bounding surfaces. The equilibrium shapes of undoped sapphire and Pt have been assessed experimentally; the literature will be reviewed to provide a basis for comparison for the present study of sapphire-Pt interfaces.

The equilibrium shape of cavities in undoped sapphire at 1600°C has been determined experimentally by two independent groups of researchers to consist of **c**$(0001)_\alpha$, **a**$\{1\bar{2}10\}_\alpha$, **r**$\{10\bar{1}\bar{2}\}_\alpha$, **s**$\{10\bar{1}1\}_\alpha$, and **p**$\{1\bar{2}13\}_\alpha$ planes [50-52]. The reported relative surface energies of undoped sapphire are summarized in Table 1. The disparity in the surface-energy hierarchy was attributed to differences in impurities in the undoped crystals, a view reinforced by more recent work [58]. Studies of the equilibrium cavity shapes in intentionally doped sapphire at 1600°C [50, 59, 60] have

revealed that dopants can change the surface-energy hierarchy, and either increase or decrease the relative surface energy range. The **m**$\{10\bar{1}0\}_\alpha$ plane does not appear in the equilibrium shape at 1600°C, although it has been predicted to appear from first-principles calculations [53-55]. Instability of the **m** plane was inferred from observations of **m** sapphire annealed at 1400°C in air [56, 57], from Wulff-shape experiments at 1600°C and 1800°C [52], and from pore-channel instability experiments at 1600°C [36, 37]. Recent work by Curiotto and Chatain [58] has suggested that selected background impurities may destabilize **m** surfaces, and that clean **m** surfaces may be stable at 980°C.

The results of surface-energy and Wulff-shape studies for Pt show a broad range of equilibrium shapes, reflective perhaps of the wide temperature range examined ($\leq$ 350°C to 1500°C) and differences in impurities and ambient atmospheres that can affect the relative surface energies. Lee *et al.* [61] annealed micron-sized Pt particles at 1200°C in an atmosphere of 10^{-7} torr (1.3×10^{-5} Pa) oxygen, a level high enough to getter carbon, but sufficiently low to result in negligible oxygen adsorption on the surfaces. The equilibrium shape was nearly spherical with small {100} and {111} facets. The specific surface energies of {100} and {111} relative to the curved surfaces were ≈ 0.96 and ≈ 0.99. In contrast, in the presence of carbon, a cubo-octahedral shape resulted. Lee *et al.* suggest that some earlier Wulff shape and relative surface energy determinations of high-purity metals were affected by adsorbates. McLean and Mykura [62] measured the orientation dependence of the specific surface energy in high-purity Pt from 920°C to 1600°C using a twin-boundary groove technique. Measurements in a 10^{-5} torr (1.3×10^{-3} Pa) vacuum showed a progressive decrease in the surface-energy anisotropy as temperature increased; at 1500°C the ratio of the maximum to minimum surface energy was 1.078, with {111} surfaces having the lowest energy. Roughening of the {100} surface at 1350°C was suggested. Annealing in air at 1100°C reduced the surface energies, and preferential oxygen adsorption to {100} and {110} surfaces was inferred. Consistent with these observations, Lee *et al.* suggested facet-to-facet variations in the heat of adsorption of gases could produce significant atmosphere-induced changes in the Wulff shape, as recently demonstrated [63].

Adsorbates can also alter the absolute and relative interfacial energies in a metal-ceramic system. For metal-oxide interfaces, the oxygen activity in the annealing atmosphere is particularly

important. As an example, the equilibrium shapes of solid MgO precipitates produced by internal oxidation of a solid (Cu,Mg) alloy [42], and of liquid Cu precipitates produced by internal reduction of Cu-doped MgO [42, 43] were studied as a function of oxygen activity at fixed temperatures. The equilibrium shapes changed significantly over the oxygen-activity range of metal-oxide coexistence. In the work to be described, samples with near-surface Pt precipitates are annealed in air; the diffusion distance is believed to be sufficient to allow the precipitates to equilibrate with the ambient oxygen activity. We are unaware of any prior study that quantifies the interfacial-energy anisotropy between Al_2O_3 and Pt. However, interfacial anisotropy may be inferred from the work of McLean and Hondros [33] on grain-boundary grooving behavior between polycrystalline Al_2O_3 and polycrystalline Pt annealed in air at 1240°C to 1540°C. The authors comment that some interfaces faceted; this implies that others did not.

The Wulff theorem, Eqn. (1), is valid for crystalline solids in contact with a vapor or liquid phase. If one considers instead a crystalline second phase embedded in a crystalline matrix, both the interfacial energy of the particle, and the elastic strain energy can contribute to the total energy. When the interfacial-energy term is dominant, the equilibrium shape approaches one that minimizes the total interfacial energy. This limiting minimum interfacial-energy shape is given by the Wulff construction, as defined in Eqn. (1). Notably, for this limiting case, when edge-energy effects are negligible, the shape (for a fixed OR) is independent of the particle volume.

When the strain-energy term is dominant, the shape approaches that which minimizes the elastic-energy contribution. Since calculating the elastic field and elastic energy of arbitrarily shaped particles is difficult, calculations have often focused on specific classes of geometric shapes to make the problem more tractable [64-72]. Efforts to predict the shape minimizing the elastic strain energy of an isolated coherent particle often apply the method of Eshelby [65, 66] to ellipsoidal particles. Lee *et al.* [67] analyzed elastically anisotropic precipitates and matrices with elastic properties of selected cubic metals. When the (ellipsoidal) precipitate was either much harder or much softer than the matrix, the optimum shape was similar to that predicted for elastically isotropic precipitate-matrix combinations with similar relative properties independent of OR. However, when the precipitate and matrix had more similar properties, a wider range of OR-sensitive results could be

obtained. As precipitate-matrix pairs with differing crystal structures and symmetries were evaluated, shape trends were more difficult to identify.

For an isolated coherent particle with a misfit strain e_{ij}^{T}, Johnson and Voorhees [69] expressed the sum of the interfacial and elastic strain energies at constant particle volume, E_t as

$$E_t = \int_A \gamma(n) dA - \tfrac{1}{2}\int_V \sigma_{ij} e_{ij}^{T} dV \qquad (2)$$

Since the interfacial-energy contribution scales with the particle interfacial area and the strain contribution with the particle volume, the relative importance of the two contributions is size dependent. With increasing particle size, the relative interfacial energy contribution decreases and the strain-energy contribution increases. One metric used to weigh the relative contributions of the strain energy and interfacial energy is provided by a parameter L, defined as $\varepsilon^2 C_{44} l^3 / \gamma l^2 = \varepsilon^2 C_{44} l / \gamma$, where ε represents a characteristic strain, C_{44} is an element of the cubic symmetric elastic constant tensor, l is a characteristic dimension taken to be $l = (3V_p/4\pi)^{1/3}$ where V_p is the precipitate volume, and γ is the (isotropic) interfacial energy. Strain-energy contributions are expected to be large when ε and l are large, γ is low, and thereby $L > 1$. For a given system, the value of L scales with the particle size.[†] Thus, a transition from a shape approaching the Wulff shape to that dictated by strain-energy minimization can be expected, and unlike a strain-free particle, the equilibrium shape of a strained particle will be particle-size dependent.

Transitions in the interface structure can also affect the equilibrium shape. As one transitions from coherent to semicoherent to incoherent interfaces, the formulation of the strain energy changes. Shear stresses acting across an incoherent interface are assumed to be relieved by interfacial sliding, and the material inside the precipitate is expected to behave like a fluid under hydrostatic stress. Nabarro [64] has shown for an elastically isotropic incoherent ellipsoidal inclusion the elastic strain energy can be minimized by adopting a disk shape. Prolonged annealing, at temperatures where diffusion in the matrix occurs, can relieve the stresses due to misfit, and the shape will again

[†] As a point of reference, Voorhees *et al.* [70] calculated the equilibrium shapes of a solid particle with an isotropic interfacial energy and elastic coefficients of Ni_3Al in a (NiAl) matrix for values of L = 0, 3, and 5. When L = 0, the 2–D morphology is circular; when L = 3 and 5, a progressively more distorted squarish equilibrium shape results. If the Wulff theorem were (inappropriately) applied to the latter two shapes, apparent variations in the relative interfacial energies of $\approx \pm 5\%$ and $\approx \pm 8\%$ about the mean interfacial energy would incorrectly be inferred for the cases where L = 3, and L = 5, respectively.

be the Wulff shape, given by Eqn. (1).

In the most general case, where the elastic properties of the inclusion and matrix are anisotropic and differ, and the interfacial energy is anisotropic and varies with the OR, identifying the preferred OR and the particle shape becomes increasingly difficult. A number of crystallographic models have been proposed that link precipitate shapes and ORs and provide guidance on the relationship between OR, shape and strain energy. The underlying criteria have been compared in a review by Dahmen [73]. One is based on the premise that particle dimensions tend to be inverse to the magnitude of the transformation strain; a second proposes that precipitates are bounded by unrotated planes; a third proposes that interfaces lie parallel to the planes of three independent dislocation loop arrays that are necessary to accommodate the strain. They predict differing degrees and types of facets, but broadly similar shapes. Interfacial-energy anisotropy is not considered.

Since the strain and interfacial relationships depend on the OR, precipitate morphology also depends on the OR. It is expected precipitates with different ORs will have unique equilibrium morphologies. Identifying the crystallographic symmetry elements of a precipitate in a matrix can help define the experimental routine required to fully characterize the precipitate morphology. Kalonji and Cahn [74, 75] described the intersection of symmetry elements of matrix and precipitate phases as the group of the Wulff plot, which gives the orientation dependence of physical properties of interfaces between arbitrarily oriented crystals. Their application of group theory indicated the intersection must be one of the thirty-two crystallographic groups common to both crystals. For the case of two different crystal structures, the symmetry group of two crystals together "is the highest common subgroup of the symmetry groups of the objects."

Sapphire is in space group R$\bar{3}$c and point group $\bar{3}$m, while Pt is face-centered-cubic and in space group Fm$\bar{3}$m and point group m$\bar{3}$m. Several precipitate orientations have been identified for Pt precipitates in sapphire [76], including $\mathbf{c}(0001)_{\alpha}||(111)_{Pt}$; $[10\bar{1}0]_{\alpha}||[1\bar{1}0]_{Pt}$. For this OR, which is observed in Pt films on sapphire [26, 77, 78], the $\bar{3}$ rotation axes are the only coincident symmetry elements; thus the group of the Wulff plot is the $\bar{3}$ point group; there are two variants for this OR.

2.2 *Kinetics of and limitations to morphological equilibration*

While the equilibrated shape of a crystal (or a void in a crystal) can provide information on

relative surface energies, in practice, morphological equilibration is very difficult to achieve in solids. In the present work it is of interest to estimate the time required for Pt inclusions of the size under investigation (<50 nm in diameter) to reach an equilibrium shape in sapphire that is within experimental error. Key issues are feature size and evolution mechanisms. Shape changes to metal-ceramic interfaces potentially involve contributions from multiple transport mechanisms. These may include volume self-diffusion of the metal, self-diffusion in the ceramic, diffusion of metal though the ceramic, diffusion of the chemical species of the ceramic through the metal, and interfacial diffusion of the metal and ceramic. If no voids are to form, the fluxes of the chemical species must be in fixed proportions, and the overall evolution rate is limited by flow of the slowest diffusing specie moving along its fastest transport path.

Unfortunately, little transport information is available specific to the Pt/sapphire system. McLean and Hondros's study of grain-boundary grooving kinetics along α-Al_2O_3/Pt interfaces annealed in air [33] provides the closest parallel to the present study. The authors concluded volume diffusion was the rate-controlling transport mode over the temperature range examined (1240-1540°C). An increase in activation energy with increasing temperature at ≈1410°C was associated with a change in the rate-controlling specie or path or both. They suggested behavior was limited by Al or O diffusion in Pt below 1410°C and by Al or O diffusion in Al_2O_3 above 1410°C. However, the activation energies they reported below 1410°C exceed those measured for the diffusivity-solubility product for O in O-doped Pt [80] and for diffusion of Al in Pt-rich (PtAl) alloys [81]. Reconciling observed activation energies with diffusion data is problematic because the (defect) chemistries and experimental conditions generally differ. Relevant diffusion studies in metals would require that both Al and O be in solution. For Pt in equilibrium with Al_2O_3 the activities of Al (a_{Al}) and O (a_O) dissolved in Pt would need to be related such that $a_{Al}^2 a_O^3$ = constant and the activation energy might superficially be expected to coincide with values for either Al or O diffusion within an α-Al_2O_3 matrix. A recent review of diffusion in α-Al_2O_3 [82] provides a compilation and analysis of reported diffusivities. None of the data for Al or O volume diffusion in undoped α-Al_2O_3 fit the findings of McLean and Hondros well; the diffusivities are much too low to account for the observed grain-boundary grooving rates. However, measurements of the Pt diffusivity in α-Al_2O_3

[83] show that Pt is soluble to some degree, and dissolved Pt may alter both the rate of and activation energy for O and Al diffusion. It is also possible that other transport mechanisms played a role.

Herring scaling laws [79] for self-similar shape changes indicate that the time for shape equilibration scales with a characteristic crystal dimension, l, raised to a power n that depends on the transport mechanism. For volume-diffusion $n = 3$, while for processes controlled by surface (or interface) diffusion evolution, $n = 4$. Scaling arguments suggest that at sufficiently fine size, the evolution is limited by interfacial diffusion.* Diffusion-controlled decay of periodic surface profiles [84-86] and shape relaxation of strain-free particles are strongly size-dependent processes, and the scaling laws apply. Thus, in contrast to grain-boundary grooving, surface or interfacial diffusion become increasingly important as the characteristic length scale over which diffusion occurs is reduced. Models of shape relaxation based on interfacial diffusion were thought to be appropriate for the fine precipitate size in the present study. This requires an estimate of the interfacial diffusivity, since such data does not exist in the literature. Work by Saiz *et al.* [14] separated the contributions of volume and interfacial diffusion in grain-boundary grooving experiments on liquid-metal (Al, Cu, Ni, Au)/α-Al_2O_3 interfaces. They found volume-diffusion-dominated transport, and that, for systems at an oxygen partial pressure where the interfaces were believed to be stoichiometric (including systems with Ni, a group VIII metal like Pt), the interfacial-diffusion contribution was similar in magnitude to the α-Al_2O_3 surface diffusivity. In a study of periodic profile decay in solid Ni/sapphire interfaces, Henrichsen and Li [87] found that diffusion may be volume-controlled or interface-controlled depending on the sapphire orientation. The interfacial diffusivity extracted from their data is $\sim 10^{-6}$ cm^2/s at 1425°C, lying in the admittedly broad range of measured surface diffusivities of α-Al_2O_3 (summarized in [88]). For comparison, reported values of the O grain-boundary diffusivity in undoped α-Al_2O_3 [89-91] range from $\approx 5 \times 10^{-13}$ to $\approx 9 \times 10^{-12}$ cm^2/s at 1425°C.

A model for volume-conserving surface-diffusion-limited morphological equilibration for

* When strain effects are present, the scaling laws fail since the relative contributions of interfacial and strain energies to the driving forces for mass flow become size dependent.

several geometries was developed by Kitayama *et al.* [92] and experimentally tested [34]. This model was extended to estimate the time for a Pt precipitate in sapphire with a non-equilibrium shape to achieve an equilibrated shape by interfacial diffusion, and thus, whether diffusion-limited morphological equilibration would occur in experimentally accessible times. The model for evolution of a flattened cylinder to a cylinder with an aspect ratio of 1 was used because it reasonably approximated the shape of Pt precipitates that form in sapphire. However, the details of the geometry (whether a parallelepiped or a cylinder), did not impact the relaxation time significantly [34].

The calculation was performed for a cylinder with an initial diameter-to-height (aspect) ratio of 4 to relax to an aspect ratio of 1.01 at 1600°C. The temporal approach to an aspect ratio of 1 is asymptotic; times to reach an aspect ratio of 1.01 were calculated. An aspect ratio of 1.01 was taken to be experimentally indistinguishable from that of a fully equilibrated nanoparticle. The initial aspect ratio of 4 was chosen because tabular Pt precipitates formed in sapphire during annealing at lower temperature (1000-1200°C) were not observed to exceed an aspect ratio of 4.

Using an interfacial diffusivity of 1.8×10^{-7} cm^2/s, which is in the middle of the reported surface diffusivities at 1600°C [88], cylinders under 100 nm in (final) diameter are expected to relax to a nearly equiaxed shape within <5 s. A more conservative estimate for interfacial diffusivity, in which it is equated to the lowest reported oxygen grain-boundary diffusivity in undoped α-Al_2O_3 at 1600°C, $D_{gb} \approx 5 \times 10^{-10}$ cm^2/s, yields a relaxation time of <0.5 h. Since volume and interfacial transport are not mutually exclusive, if volume transport is also significant for solid metal/α-Al_2O_3 interfaces, it would decrease the time to morphological equilibration.

Additional barriers exist to the morphological changes in faceted crystals [93]. When a time-independent source of ledges such as a screw dislocation is present, migration can be diffusion-limited. If a ledge-producing source is absent, facet movement requires the nucleation and lateral growth of atomic-height patches of atoms, or the nucleation and growth of atomic-height cavities in layers. Thus, the movement of facets can be nucleation-rate limited. As the equilibrium shape is approached, the driving force for shape change decreases. When the driving force decreases sufficiently, the nucleation rate becomes vanishingly low, and shape change becomes kinetically

hindered. This has been observed in the shape equilibration of cavities in sapphire [34] and SiC [35], in liquid Pb inclusions in Al [40], and Pb crystals supported on graphite [94].

Mullins and Rohrer developed a model to quantify the nucleation energy barrier for volume-conserving shape changes of faceted crystals near their equilibrium morphology [95], and an extension of the approach treated the evolution of pores and particles far from their equilibrium shapes [96]. A significant nucleation energy barrier emerged for the creation of atomic-height patches necessary for the normal displacement of a facet that is just a few nanometers in diameter. The nucleation energy barrier scaled with the facet size and increased as the equilibrium morphology was approached. Rohrer, Rohrer, and Mullins [96] considered the evolution of partially faceted crystals (truncated spheres with both curved and parallel singular surfaces), and approaches to equilibrium that required the facet to move both towards and away from the energy barrier. For prolate shapes equilibration involves facet movement towards the particle center, and transfer of mass from the facets to the curved equatorial section. The energy barrier increased relatively slowly but could become sufficiently large to inhibit a full approach to equilibrium. When instead the facets must advance away from the crystal center during equilibration, for so-called oblate forms, the energy barrier could still be a large fraction of the maximum energy barrier even far from equilibrium. Thus a partially faceted crystal was more likely to be trapped in a non-equilibrium morphology if the faceted surfaces must advance outward, a behavior observed in Pb inclusions in Al [40]. Experimentally, if initial morphologies lie on both sides of the equilibrium shape, then a range of shapes and "scatter" in the associated γ_j/l_j values is anticipated.

Reaching an equilibrium shape is thus a multiply constrained process. Scaling-law arguments for unstrained crystals indicate that achieving an equilibrium shape in experimentally accessible times generally requires studies of fine particles, of micron scale or less. Faceting can effectively prevent the approach to equilibrium even in finer-scale crystals, and the likelihood of having a time-independent ledge source increases with particle size, creating behavior that goes counter to scaling-law expectations [17, 35]. When global equilibrium is not reached due to either scaling-law effects or faceting or both, information relating to the Wulff shape can nonetheless be extracted. It has been taken as a theorem, that only orientations that appear in the Wulff shape may occur in a locally

equilibrated portion of a microstructure [97], *i.e.*, orientations appearing in a local equilibrium may be used to identify the orientations that appear in a fully equilibrated crystal, and to assess relative energies from a constrained local-equilibrium configuration *e.g.*, [40, 96].

3. Experimental Procedures

Four optical-grade, 99.996%-pure sapphire wafers with the large face coinciding with either a $\mathbf{c}(0001)_\alpha$ or an $\mathbf{m}\{10\bar{1}0\}_\alpha$ plane to within 1° were implanted with a $1 \times 10^{16}\,Pt^+/cm^2$ at an angle 7° to the normal of the large face. An implantation energy of 600 keV was used, which, based on SRIM/TRIM [98] simulations, is expected to result in a peak Pt concentration 96 nm below the sapphire surface. A **c** and an **m** substrate were implanted at room temperature; a second set was implanted while cooled to liquid nitrogen ($l\!N_2$) temperature. The dose and distribution of Pt were confirmed by Rutherford backscatter spectroscopy (RBS) performed on pieces of sapphire for each implantation condition. Post-implantation annealing in air for 100 h at 1600°C on 3 mm-wide pieces of the substrates was used to induce precipitation and anneal out implantation damage. The damage and dislocations present at the initial stages of annealing were expected to facilitate equilibration of the oxygen activity in the implanted layer with the ambient. Based on the estimate that diffusion-limited morphological equilibration is possible in <0.5 h for precipitates 100 nm in diameter at 1600°C, 100 h was seen as adequate for shape relaxation to occur, even if the estimate is off by several orders of magnitude. The ramp rate up to and down from 1600°C was 5°C/min.

After annealing, the substrates were characterized with x-ray diffraction (XRD) after which the specimens were prepared in electron-transparent foils in cross-section and plan view. Conventional transmission electron microscopy (CTEM) imaging and diffraction was carried out using a JEOL 200CX operated at 200 keV. Diffraction patterns on zone axes of the sapphire matrix were used to find ORs of groups of Pt precipitates with respect to the sapphire matrix. Conventional two-beam and centered-beam-zone-axis bright-field (BF)/dark-field (DF) imaging was used to determine the orientation of individual Pt precipitates with respect to the sapphire before morphological measurements were made. Orientations of precipitates imaged in high-resolution transmission electron microscopy (HRTEM) were determined from fast Fourier transforms of the images. Conventional BF images and HRTEM phase-contrast images from the [0001], $<10\bar{1}0>_\alpha$ and

$<1\bar{2}10>_\alpha$ zone axes were used to characterize the morphology of precipitates with $\mathbf{c}(0001)_\alpha||(111)_{Pt}$; $[10\bar{1}0]_\alpha||[1\bar{1}0]_{Pt}$ through the identification of faceted Pt-Al_2O_3 interfaces. Precipitate dimensions in the directions normal to the facets or low-index sapphire planes were measured on calibrated CTEM images. Phase-contrast HRTEM was performed using either a Philips CM300/FEG UT or an FEI F20 UT Tecnai microscope.

4. Results and Discussion

Based on the RBS spectra (Figure 1), the Pt doses for implantation at room temperature and at lN_2 temperature were 1.2×10^{16} Pt/cm^2 and 1.3×10^{16} Pt/cm^2, respectively, with an uncertainty of ±5%. The figure inset gives the Pt distribution as a function of depth; the peak concentration occurs close to the depth anticipated from the SRIM/TRIM simulation. The XRD data [76] has shown that multiple, non-random orientations result from either processing method and that the prevalent orientation depends on the processing parameters, as reported by others [99]. The orientation $\mathbf{c}(0001)_\alpha||(111)_{Pt}$; $[10\bar{1}0]_\alpha||[1\bar{1}0]_{Pt}$ – the highest symmetry orientation observed in these specimens – occurred with high frequency in sapphire that was partially amorphized during implantation and which forms a transition alumina during annealing and before the damaged matrix transforms back into sapphire. For the implantation dose used here, extensive amorphization occurred only in the lN_2-cooled sapphire, but substrates implanted at both implantation temperatures were used for precipitate characterization.

Figures 2–5 show CTEM and HRTEM zone-axis images of the type used to determine the precipitate morphologies. The morphology of precipitates with $\mathbf{c}(0001)_\alpha||(111)_{Pt}$; $[10\bar{1}0]_\alpha||[1\bar{1}0]_{Pt}$ may be described as partially faceted with planar interfaces connected by curved interfaces. The facets were identified relative to the sapphire matrix by identifying orientation relative to the sapphire atomic planes in HRTEM images or in CTEM by determining the angular orientation relative to the sapphire orientation identified by diffraction patterns. Faceted interfaces were identified coinciding with the following low-index planes of the sapphire matrix: $\mathbf{c}(0001)_\alpha$, $\mathbf{r}\{10\bar{1}\,\bar{2}\}_\alpha$, $\mathbf{s}\{10\bar{1}1\}_\alpha$, $\{10\bar{1}\,\bar{5}\}_\alpha$, $\{10\bar{1}4\}_\alpha$, $\mathbf{a}\{1\bar{2}10\}_\alpha$, and variants of $\mathbf{p}\{1\bar{2}13\}_\alpha$, $\{1\bar{2}16\}_\alpha$, and

$\{1\bar{2}19\}_\alpha$.* Of these, the five orientations preceded by a bold letter, have been experimentally determined to be part of the equilibrium shape of sapphire [50-52] at 1600°C. Curved interfaces between $\mathbf{r}\{10\bar{1}\,\bar{2}\}_\alpha$ and $\mathbf{s}\{10\bar{1}1\}_\alpha$ facets (when viewed along $<1\bar{2}10>_\alpha$ direction) included interfaces coinciding with $\mathbf{m}\{10\bar{1}0\}_\alpha$, but there is some ambiguity as to whether or not very small **m** facets are present. Rather than identifying **m**-oriented interfaces as "facets", it may be more accurate to assert that when in contact with Pt, this is not a missing orientation, as is the case for sapphire in contact with a vapor phase under a broad range of experimental conditions. Only three of the above-mentioned sapphire planes coincide exactly with a low-index Pt plane for this OR. Those are $\mathbf{c}(0001)_\alpha$, $\mathbf{a}\{1\bar{2}10\}_\alpha$, and $\mathbf{m}\{10\bar{1}0\}_\alpha$ with interfacial relationships $\mathbf{c}(0001)_\alpha||(111)_{Pt}$; $[10\bar{1}0]_\alpha||[1\bar{1}0]_{Pt}$, $\mathbf{a}(1\bar{2}10)_\alpha||(1\bar{1}2)_{Pt}$; $[0001]_\alpha||[111]_{Pt}$, and $\mathbf{m}(10\bar{1}0)_\alpha||(1\bar{1}0)_{Pt}$; $[0001]_\alpha||[111]_{Pt}$, respectively. To aid visualization of the sapphire and Pt interfacial relationships, indexed, simulated zone-axis diffraction patterns are shown in Figure 6. In Figure 6a, one can see $\mathbf{r}\{10\bar{1}\,\bar{2}\}_\alpha$, $\mathbf{s}\{10\bar{1}1\}_\alpha$, and $\{10\bar{1}4\}_\alpha$ are within ~1° of being coplanar with low-index planes of Pt. In Figure 6b, one can see the crystallographic differences between the $\{1\bar{2}1\ell\}_\alpha$ and $\{1\bar{2}1\bar{\ell}\}_\alpha$ orientations with respect to Pt and that these low-index sapphire planes are several degrees away from being coplanar with low-index Pt planes (with non-zero structure factors) in the same zone axis.

The identification of facets on these nanoprecipitates presented technical challenges, because the facets are only a few nanometers across and difficult to discern in CTEM and even in HRTEM because the interfaces are buried. The faceted interfaces coinciding with $\mathbf{c}(0001)_\alpha$, $\mathbf{a}\{1\bar{2}10\}_\alpha$, $\mathbf{r}\{10\bar{1}\,\bar{2}\}_\alpha$, $\mathbf{s}\{10\bar{1}1\}_\alpha$, $\{10\bar{1}\,\bar{5}\}_\alpha$, $\{10\bar{1}4\}_\alpha$, and variants of $\mathbf{p}\{1\bar{2}13\}_\alpha$ appear with little ambiguity, cf. Figures 2–5. Interfaces coinciding with the variants of $\{1\bar{2}16\}_\alpha$ and especially $\{1\bar{2}19\}_\alpha$ are difficult to resolve; the interfaces in this region sometimes appear faceted and sometimes curved.† The error in the angular measurement of very small facets on CTEM images could be several degrees, which is problematic when trying to differentiate $\{1\bar{2}16\}_\alpha$ and $\{1\bar{2}19\}_\alpha$ interfaces that have an angular separation of 11°. In spite of these difficulties, there are instances in which these facets are

* For sapphire, $\{1\bar{2}1\ell\}_\alpha$ is crystallographically equivalent to $\{1\bar{2}1\bar{\ell}\}_\alpha$. However, for the precipitate orientation relationship examined, interfaces bound by $\{1\bar{2}1\ell\}_\alpha$ and $\{1\bar{2}1\bar{\ell}\}_\alpha$ differ because the sapphire contacts different Pt orientations.
† The differences could be due to differences in $\{1\bar{2}1\ell\}_\alpha$ /Pt and $\{1\bar{2}1\bar{\ell}\}_\alpha$/Pt interfacial relationships, non-optimal imaging conditions, or lack of complete convergence on an equilibrium shape.

discerned, cf. Figures 3 and 4b, but the differentiation of two possible precipitate variants is not made in CTEM or in HRTEM. Thus, the different $\{1\bar{2}1l\}_\alpha$ interfacial variants are not distinguished.

Measurements of the dimensions, w, of the precipitates normal to faceted interfaces and $\mathbf{m}\{10\bar{1}0\}_\alpha$ interfaces were made. Since the facets coincided with low-index planes of the sapphire matrix, the facets are described by the sapphire indices for brevity, $w_{(hkil)_\alpha}$. When viewed along $[0001]_\alpha$, as in Figure 2, the precipitates appear as dodecagons consisting of alternating $\mathbf{a}\{1\bar{2}10\}_\alpha$ facets and curved interfaces that include $\mathbf{m}\{10\bar{1}0\}_\alpha$ which lie parallel to the viewing direction. Figure 7a shows a plot of $w_{\mathbf{a}(11\bar{2}0)_\alpha}$ versus $w_{\mathbf{a}(1\bar{2}10)_\alpha}$ for measurements made from the $[0001]_\alpha$ zone axis. The data points fall on a line with a slope of 1, indicating the particles are equiaxed when observed in this direction. Since the $[1\bar{2}10]_\alpha$ and $[11\bar{2}0]_\alpha$ directions in precipitates with the orientation $\mathbf{c}(0001)_\alpha||(111)_{Pt}$; $[10\bar{1}0]_\alpha||[1\bar{1}0]_{Pt}$ are crystallographically identical, it is expected that $w_{\mathbf{a}(11\bar{2}0)_\alpha} / w_{\mathbf{a}(1\bar{2}10)_\alpha} = 1$ if the shape has equilibrated. The normalized $w_{(hkil)_\alpha}$ measurements made from the $[0001]_\alpha$ zone axis are given in the first two lines of Table 2. Note that the average normalized precipitate dimensions normal to $\mathbf{m}\{10\bar{1}0\}_\alpha$ planes are only 2% larger than the precipitate dimensions normal to $\mathbf{a}\{1\bar{2}10\}_\alpha$ planes. The magnitude of the deviation from a value of unity for the $\mathbf{m}\{10\bar{1}0\}_\alpha$ planes is only slightly more than the standard deviation of the measurement set.

The $w_{(hkil)_\alpha}$ for precipitates viewed along the $<10\bar{1}0>_\alpha$ and $<1\bar{2}10>_\alpha$ zone axes are plotted against $w_{\mathbf{a}(1\bar{2}10)_\alpha}$ and $w_{\mathbf{m}(10\bar{1}0)_\alpha}$, respectively, in Figures 7b and 7c. The results include a range of distinct orientations, with measurements taken from precipitates with dimensions ranging from ~10 nm to 45 nm. The results can conveniently be divided into two groups with distinct characteristic features. Group 1 includes all interfaces or orientations that do not involve $\mathbf{c}(0001)_\alpha||(111)_{Pt}$ interfaces and Group 2, the interfaces that do. In Tables 2 and 3, entries from Group 1 are unshaded, while those from the second are shaded in grey to facilitate comparison.

For interfaces in Group 1, data in Tables 2 and 3 show that the average normalized dimensions over the range of particle size studied are close to unity (see Figures 7a-c). For Group 1, Table 2 includes $w_{\mathbf{p}\{1\bar{2}13\}_\alpha}$, and $w_{\{1\bar{2}16\}_\alpha}$ measurements from the $[10\bar{1}0]_\alpha$ zone axis normalized by $w_{\mathbf{a}\{1\bar{2}10\}_\alpha}$, and $w_{\mathbf{r}(10\bar{1}\bar{2})_\alpha}$, $w_{\mathbf{s}\{10\bar{1}1\}_\alpha}$, $w_{\{10\bar{1}\bar{5}\}_\alpha}$, and $w_{\{10\bar{1}4\}_\alpha}$, measurements from the $[1\bar{2}10]_\alpha$ zone axis normalized by $w_{\mathbf{m}\{10\bar{1}0\}_\alpha}$. Measurements of $w_{\mathbf{a}\{1\bar{2}1l\}_\alpha}$ and $w_{\mathbf{a}\{1\bar{2}1\tilde{l}\}_\alpha}$ in individual precipitates varied little

and were often the same within experimental error, even though the interfacial crystallography differed. As a result, and for simplicity, the measurements of such pairs are combined in Figure 7 and Table 2. For measurements along $<1\bar{2}10>_\alpha$, normalization by the 2% larger $w'_{\mathbf{m}\{10\bar{1}0\}_\alpha}$ (relative to $w'_{\mathbf{a}(1\bar{2}10)_\alpha}$) results in slightly lower normalized values. For Group 1, the deviations of the average normalized values from unity are generally less than the standard deviation.

The characteristics of interfaces with $\mathbf{c}(0001)_\alpha||(111)_{Pt}$, Group 2, deviate substantially from those of Group 1 interfaces, as is evident in Figures 7b-c and in Tables 2 and 3. The data sets for $w'_{\mathbf{c}(0001)_\alpha}$ and $w'_{\mathbf{a}(1\bar{2}10)_\alpha}$ were increased by imaging and measuring $w'_{\mathbf{c}(0001)_\alpha}$ and $w'_{\mathbf{a}(1\bar{2}10)_\alpha}$ for 29 additional particles. The plot of $w'_{\mathbf{c}(0001)_\alpha}$ versus $w'_{\mathbf{a}(1\bar{2}10)_\alpha}$ for 47 different precipitates (Figure 7d.) shows no clear trend attributable to size effects for the range of precipitates measured, 10 to 50 nm. There are no instances in which the normalized dimension substantially exceeds unity, the average normalized dimensions are discernibly below unity, and the scatter in the values is much more substantial, evidenced by a standard deviation at least twice that of any Group 1 measurement. For comparably sized particles in the middle of the size range examined, normalized dimensions can vary from 0.66 to 0.99. The data is consolidated in Table 3 by renormalizing all measurements by $w'_{\mathbf{a}(1\bar{2}10)_\alpha}$. The measurements indicate all Group 1 interfaces have normalized dimensions that vary from unity by 2% or less while Group 2 interfaces, bound by **c** sapphire planes, show a larger variation from unity and larger variability.

Size-dependent variation of the normalized values of $w'_{\mathbf{c}(0001)_\alpha}$ could have multiple causes, but the failure to converge to a single value even at fixed precipitate size suggests the equilibrium shape has not been reached. The observed variations of shape impose constraints on the extent of the analysis. However, potential causes of the behavior are of interest, and specific aspects of the results warrant further analysis. It is useful to address the potential roles of strain energy, possible errors in the diffusion analysis, and the role of ledge nucleation and nucleation energy barriers on the results.

To this stage, the morphologies have been discussed purely in terms of their dimensional characteristics. The lattice mismatch between Pt and Al_2O_3 has the potential to produce elastic stresses and strain-energy contributions that could alter the driving forces for mass flow during processing and the ultimate equilibrium shape. In such situations, the relative $w'_{(hkil)_\alpha}$ values do not

translate to relative interfacial energies. In analyses of this coupled strain energy-surface energy minimization problem [70], the relative magnitudes of the (volumetric) strain-energy and surface-energy contributions to the equilibrium shape can be assessed by evaluating the previously described parameter $L = \varepsilon^2 C_{44} l/\gamma$. Strain-energy contributions are expected to be large when ε and l are large, γ is low, and thereby $L > 1$. For nanoscale Pt precipitates in sapphire, l is small, and γ is relatively large. The relative contribution of strain energy to the shapes of the Pt particles examined can be estimated by taking the largest particles ($l \approx 25$ nm), and assuming that during annealing at 1600°C the particles are subject to a time-independent lattice mismatch or strain ε of ≈0.0567 for the $(111)_{Pt}$-$(0006)_{\alpha}$ misfit and ≈0.0195 for the $(220)_{Pt}$-$(30\bar{3}0)_{\alpha}$ misfit. The parameter C_{44} has been measured up to ≈1127°C [100], where it has a value of 7×10^{10} N/m^2; the actual value at 1600°C is expected to be lower. A value of 1.05 J/m^2 has been reported for the Al_2O_3/Pt interfacial energy on the basis of grain-boundary grooving experiments [33]; the authors noted the value is low in comparison to then-contemporary measurements of other ceramic/metal interfacial energies. More recently, Sadan and Kaplan [16] assessed the energy of $\mathbf{c}(0001)_{\alpha}||(111)_{Au}$ and $\mathbf{c}(0001)_{\alpha}||(100)_{Au}$ interfaces and reported values of 2.15 and 2.18 J/m^2, respectively. Overestimating ε and C_{44}, taking the maximum value of l, and 1.05 J/m^2 for γ, and assuming that the interface is coherent, one obtains $L = 5.36$ for the $(111)_{Pt}$-$(0006)_{\alpha}$ misfit and $L = 0.634$ for the $(220)_{Pt}$-$(30\bar{3}0)_{\alpha}$ misfit. HRTEM of precipitate interfaces shows that even $(0001)_{\alpha}||(111)_{Pt}$ interfaces with small in-plane misfits are, at most, only partially coherent, with defect structures forming apparently to accommodate the misfit. The accommodation of lattice misfit at the interface diminishes the role of strain energy in determining equilibrium precipitate morphology. Additionally, XRD data [76] did not show evidence of strain in the Pt for the $(111)_{Pt}$-$(0006)_{\alpha}$ misfit (within experimental error). Although strain energy could have some influence on the equilibrium shape, the data fails to show any supporting size-dependent trends suggesting it is a major factor. Given the presence of strain-accommodating defects even when $L < 1$, we anticipate that strain-energy effects are minor, and a kinetic analysis treating the simpler problem of diffusion-controlled shape relaxation driven by a reduction in interfacial energy provides a useful estimate of the shape-equilibration times.

The precipitates formed during lower-temperature post-implantation annealing span a range

of sizes and shapes. One possible interpretation of the scatter in the normalized values of $w_{\mathbf{c}(0001)_\alpha}$ is that variations in the initial morphologies impose variations in the equilibration times, and cause the observed variations in the final morphologies. We believe this is unlikely for interfacial diffusion-controlled evolution. The estimated relaxation time of <0.5 h at 1600°C assumes a particle size twice that of the largest particle measured, the most extreme initial deviation from an equiaxed shape observed, and excludes contributions from other transport mechanisms. In this regard, McLean and Hondros' work [33] suggests dominant lattice diffusion contributions to grain-boundary groove growth from 1240 to 1540°C, thus it is plausible there are significant additional contributions to the mass flow. Using surface diffusivity as an estimate for the operative diffusion coefficient, a $>10^4$ reduction is needed to rationalize the lack of convergence of $w_{\mathbf{c}(0001)_\alpha}$ values. Moreover, for a model based on diffusion control, it would be difficult to rationalize the convergence of normalized $w_{(hkil)_\alpha}$ values for Group 1 interfaces over the same range of precipitate size.

The role of facets in inhibiting kinetic processes has been recognized for decades. Rohrer *et al.* [96] assessed the role that nucleation energy barriers could have in kinetically inhibiting the development of the Wulff shape in fully or partially faceted crystals of nonequilibrium morphology. Their review of the literature through 2001 provides examples of studies where the observed behavior was likely to have been affected by a nucleation energy barrier. To these, one can add studies of shape equilibration of Cu particles [17], and voids in SiC [35], and morphological evolution of pore channels [36, 37], and metal-filled channels in sapphire [41]. The present observations of "scatter" in the $w_{\mathbf{c}(0001)_\alpha}$ values seem consistent with that specific interface being most prone to the effects of nucleation-limited motion. Several other findings also seem to support this view. For the OR examined here, $\mathbf{c}(0001)_\alpha||(111)_{Pt}$, three sapphire planes, the **c**, **a**, and **m** planes, are found to be exactly parallel to low-index planes in Pt. As discussed, there is some uncertainty as to whether **m** facets form; it is merely observed that interfaces involving the **m** plane are present. For the **a** planes, reference to Figures 3 and 4 suggests that even in the larger particles, the **a** facet is small. Since the nucleation energy barrier scales linearly with facet size, the **a** facets may remain in the range where nucleation barriers are more easily overcome. Also, the **a** facets are impinged upon by smoothly curved sections with a low contact angle, suggesting a low step energy.

For this OR, the **c** facet tends to be the largest, and is impinged by other facets or curved sections at a sufficiently high angle to create a sharp edge, indicating missing orientations. This is consistent with a picture in which local, circumferential shape adjustment is rapid, but movement of the **c**-facets limits global equilibration, a scenario that would explain the consistency of the normalized $w_{(hkil)_\alpha}$ values for Group 1 interfaces.

A corollary of the proposed explanation is that even when $w_{\mathbf{c}(0001)_\alpha}$ deviates from its equilibrium value, a local equilibrium morphology is achieved in the "edge" segments that connect the **c**-facets. A preliminary assessment of selected particle shapes show that the edges are well approximated by circular arcs and the deviations due to faceting are minor. This suggests that if the morphology is largely dictated by the relative surface energies, the energies of the surfaces that make up the edges are similar. This is consistent with the emergence of curved interface sections, the presence of interfaces that include the **m**-plane, and the apparent similarity in the energies of $(1\bar{2}1l)_\alpha$ and $(1\bar{2}1\bar{l})_\alpha$ interfaces. The anisotropy may be somewhat larger than indicated in Tables 2 and 3, but more extensive measurements are needed to confirm this. Assuming that the data in Figure 7 includes some from particles that have reached equilibrium, the insensitivity of the normalized $w_{(hkil)_\alpha}$ values for Group 1 interfaces are consistent with this correction being small. If local equilibrium is assumed, it follows that the observed facets are part of the Wulff shape for the OR examined, and that Pt reduces the energy differences that exist in the energies of the corresponding surfaces of sapphire when in contact with vapor.† The results of Sadan and Kaplan [16] for sapphire/Au interfaces also show small variations in the interfacial energy, albeit from a more limited sampling of ORs. Studies of other fcc metals may reveal whether the behavior is more broadly observed.

A limited reassessment of the relative energies of the **c** facets to other facets, paralleling the conceptual approach used by Gabrisch *et al.* [40], and described by Rohrer *et al.* [96], shows that the contact angle for the **c**-facet is in the range of 20°-30°, which suggests that the **c**-facet energy lies

† One caution is that the samples were cooled at 5°C/min. If transport along the circumferential section is rapid, facets may develop or adjust position during cooling from 1600°C. Since anisotropy increases with decreasing temperature, this would not contradict the general view that Pt homogenizes the interfacial energies.

within the range of 0.87 to 0.94 of the energy of the Group 1 interfaces. More detailed analysis of the edge profile, as described by Gabrisch *et al.* is needed to provide a more refined estimate. The least-squares fit of the data in Table 3 generates a value of 0.86. Both values suggest that the full set of particles includes some that are approaching equilibrium from an initial geometry that is prolate with respect to the equilibrium shape while others are approaching from an oblate initial configuration. The analysis of Rohrer *et al.* suggests the nucleation energy barriers can become sufficiently large to prevent equilibrium from being reached in both situations, *i.e.*, even in cases where the facet moves towards the particle center. Thus the persistence of a bracketing spread in $w_{\mathbf{c}(0001)_\alpha}$ is anticipated in that situation. A study of particles smaller than 10 nm in size may be required to determine the equilibrium value of $w_{\mathbf{c}(0001)_\alpha}$, but would be challenging to execute.

Finally, although facets coinciding with low-index planes of sapphire are identified, the sapphire matrix does not "control" the precipitate morphology. Based on crystallographic considerations such as the group of the Wulff plot, it is expected that precipitates with different ORs will have different morphologies. Figure 8 provides an example of a precipitate with the OR $\mathbf{c}(0001)_\alpha||(110)_{Pt}$; $[10\bar{1}0]_\alpha||[1\bar{1}2]_{Pt}$. The morphology is distinct from that of the precipitates viewed from the same sapphire zone axis in Figure 2. The precipitate has a higher areal density of curved surfaces, a different symmetry, and facets where the **a** planes coincide with $\{111\}_{Pt}$. The morphology is affected by the OR and is not controlled by the precipitate or matrix alone.

5. Summary and Conclusions

The morphology of Pt precipitates in sapphire with the orientation $\mathbf{c}(0001)_\alpha||(111)_{Pt}$; $[10\bar{1}0]_\alpha||[1\bar{1}0]_{Pt}$ annealed for 100h at 1600°C in air has been determined. The morphology consists of both curved interfaces and facets; the facets coincide with low-index planes of sapphire. The low-index sapphire planes include all of those in the experimentally determined equilibrium shape of undoped sapphire [50-52] (**c**, **r**, **s**, **a**, **p**) and several that do not ($\{10\bar{1}4\}_\alpha$, $\{10\bar{1}\,\bar{5}\}_\alpha$, $\{1\bar{2}16\}_\alpha$, $\{1\bar{2}19\}_\alpha$). Although the data is not adequate to determine if faceted interfaces with $\mathbf{m}(10\bar{1}0)_\alpha||(1\bar{1}0)_{Pt}$; $[0001]_\alpha||[111]_{Pt}$ are part of the precipitate equilibrium shape, interfaces bound with $\mathbf{m}\{10\bar{1}0\}_\alpha$ are not missing, as they are in sapphire in equilibrium with a vapor phase. These observations lead to the conclusion that Pt-sapphire contact homogenizes relative interfacial

energies relative to the magnitude of surface energy anisotropy reported for sapphire.

Although calculations suggested that the anneal time and temperature were sufficient for full morphological equilibration by diffusion-controlled evolution, the precipitates did not converge on a single shape. The lack of equilibration for precipitates larger than ~10 nm diameter is believed to be due to lack of a time-independent source of ledges for interfaces with an interfacial relationship: $\mathbf{c}(0001)_\alpha||(111)_{Pt}$; $[10\bar{1}0]_\alpha||[1\bar{1}0]_{Pt}$, and the nucleation barriers to forming such ledges. The relative particle dimensions are close to unity in all directions except normal to interfaces bound by $\mathbf{c}(0001)_\alpha||(111)_{Pt}$; $[10\bar{1}0]_\alpha||[1\bar{1}0]_{Pt}$ interfaces. The precipitate dimension normal to these interfaces is ~10% smaller than in the other directions, and the values show relatively greater scatter. Such scatter would be expected if the initial particle shape distribution includes geometries that are both oblate and prolate relative to the equilibrium geometry, and nucleation energy barriers prevent full convergence on the equilibrium shape. Measurements of particle dimensions and of contact angles both suggest that the $\mathbf{c}(0001)_\alpha||(111)_{Pt}$; $[10\bar{1}0]_\alpha||[1\bar{1}0]_{Pt}$ interfaces have lower interfacial energy than others for the specific particle OR explored in this study.

Acknowledgements

This research was supported by the Metals & Metallic Nanostructures Program of the National Science Foundation through Grant No. 0805062. MKS was supported by an NSF Graduate Research Fellowship. Portions of the work by MKS were performed under the auspices of the U.S. Department of Energy by Lawrence Livermore National Laboratory under Contract DE-AC52-07NA27344. AMG acknowledges generous support from the GRF. VR acknowledges support of Nanotechnology and Functional Materials Center, Faculty of Technology and Metallurgy, University of Belgrade, Serbia. RG and MCR are supported by the Australian Research Council. All electron microscopy in this work was performed at the National Center for Electron Microscopy (NCEM), which is supported by the Office of Science, Office of Basic Energy Sciences of the U.S. Department of Energy under Contract No. DE-AC02-05CH11231. MKS and AMG thank U. Dahmen for many useful conversations over the course of this work.

References:

[1] Rühle M, Evans AG. Mater Sci Eng A 1989;107:187.
[2] Howe JM. Int Mater Rev 1993;38:233.
[3] Rühle M. J Eur Ceram Soc 1996;16:353.
[4] Ikuhara Y, Pirouz P. Microsc Res Technique 1998;40:206.
[5] Matsunaga K, Sasaki T, Shibata N, Mizoguchi T, Yamamoto T, Ikuhara Y. Phys Rev B 2006;74.
[6] Mortensen A, Jin I. Int Mater Rev 1992;37:101.
[7] Nicholas MG, Mortimer DA. Mater Sci Technol 1985;1:657.
[8] Nicholas MG. Br Ceram Trans J 1986;85:144.
[9] Loehman RE, Tomsia AP. Am Ceram Soc Bull 1988;67:375.
[10] Elssner G, Petzow G. ISIJ Int 1990;30:1011.
[11] Fernie JA, Drew RAL, Knowles KM. Int Mater Rev 2009;54:283.
[12] Eustathopoulos N, Chatain D, Coudurier L. Mater Sci Eng A 1991;135:83.
[13] Eustathopoulos N, Nicholas MG, Drevet B. Wettability at High Temperatures. Amsterdam: Pergamon; 1999.
[14] Saiz E, Cannon RM, Tomsia AP. Acta Mater 1999;47:4209.
[15] Saiz E, Cannon RM, Tomsia AP. Annu Rev Mater Res 2008;38:197.
[16] Sadan H, Kaplan WD. J Mater Sci 2006;41:5099.
[17] Chatain D, Ghetta V, Wynblatt P. Interface Sci 2004;12:7.
[18] Klomp JT. Am Ceram Soc Bull 1972;51:683.
[19] Debruin HJ, Warble CE, Moodie AF. J Mater Sci 1972;7:909.
[20] Bailey FP, Borbidge WE. In Pask JA, Evans AG (Eds.). Surfaces and Interfaces in Ceramic and Ceramic-metal Systems, vol. 14. New York: Plenum Press, 1981. p.525.
[21] Allen RV, Borbidge WE. J Mater Sci 1983;18:2835.
[22] Reimanis IE, Dalgleish BJ, Evans AG. Acta Metall et Mater 1991;39:3133.
[23] Howe JM. Int Mater Rev 1993;38:257.
[24] Dalgleish BJ, Saiz E, Tomsia AP, Cannon RM, Ritchie RO. Scripta Metall Mater 1994;31:1109.
[25] Elssner G, Korn D, Ruhle M. Scripta Metall Mater 1994;31:1037.
[26] Ramanathan S, Clemens BM, McIntrye PC, Dahmen U. Philos Mag A 2001;81:2073.
[27] Scheu C, Liu Y, Oh SH, Brunner D, Ruhle M. J Mater Sci 2006;41:7798.
[28] Scheu C, Dehm G, Mullejans H, Ruhle M. Intergranular and Interphase Boundaries in Materials, Part 1, vol. 207. Zurich-Uetikon: Transtec Publications Ltd, 1996. p.181.
[29] Scheu C. Interface Sci. 2004;12:127.
[30] Sasaki T, Mizoguchi T, Matsunaga K, Tanaka S, Yamamoto T, Kohyama M, Ikuhara Y. Appl Surf Sci 2005;241:87.
[31] Mizoguchi T, Sasaki T, Tanaka S, Matsunaga K, Yamamoto T, Kohyama M, Ikuhara Y. Phys Rev B 2006;74.
[32] Feingold AH, Li CY. Acta Metall 1968;16:1101.
[33] McLean M, Hondros ED. J Mater Sci 1971;6:19.
[34] Kitayama M, Narushima T, Glaeser AM. J Am Ceram Soc 2000;83:2572.
[35] Narushima T, Glaeser AM. J Am Ceram Soc 2001;84:921.
[36] Santala MK, Glaeser AM. Surf Sci 2006;600:782.
[37] Santala MK, Glaeser AM. Acta Mater 2008;56:1967.
[38] Willertz LE, Shewmon PG. Metall Trans 1970;1:2217.
[39] Harris PJF. Int Mater Rev 1995;40:97.

[40] Gabrisch H, Kjeldgaard L, Johnson E, Dahmen U. Acta Mater 2001;49:4259.
[41] Sugar JD, McKeown JT, Radmilovic V, Glaeser AM, Gronsky R. Acta Mater 2010;58:5332.
[42] Backhaus-Ricoult M, Laurent S. Mater Sci Forum 1999;294-6:173.
[43] Backhaus-Ricoult M. Acta Mater 2001;49:1747.
[44] Yim WM, Paff RJ. J Appl Phys 1974;45:1456.
[45] White GK, Roberts RB. Thermal expansion of reference materials: tungsten and alpha-Al_2O_3. 8th European Thermophysical Properties Conference. Baden Baden, West Germany; 1983.
[46] Kirby RK. Platinum-A thermal expansion reference material. 10th International Thermal Expansion Symposium. Boulder, CO; 1991.
[47] Arblaster JW. Platinum Metals Rev 1997;41:12.
[48] De Graef M, Dalgleish BJ, Turner MR, Evans AG. Acta Metall et Mater 1992;40:S333.
[49] Wulff G. Z Krystallogr 1901;34.
[50] Kitayama M. The Wulff Shape of Doped and Undoped Alumina. Berkeley: Department of Materials Science & Engineering, University of California; 1996.
[51] Choi JH, Kim DY, Hockey BJ, Wiederhorn SM, Handwerker CA, Blendell JE, Carter WC, Roosen AR. J Am Ceram Soc 1997;80:62.
[52] Kitayama M, Glaeser AM. J Am Ceram Soc 2002;85:611.
[53] Manassidis I, Gillan MJ. J Am Ceram Soc 1994;77:335.
[54] Gay DH, Rohl AL. J Chem Soc-Faraday Trans 1995;91:925.
[55] Marmier A, Parker SC. Phys Rev B 2004;69:115409.
[56] Heffelfinger JR, Bench MW, Carter CB. Surf Sci 1995;343:L1161.
[57] Heffelfinger JR, Carter CB. Surf Sci 1997;389:188.
[58] Curiotto S, Chatain D. Surf Sci 2009;603:2688.
[59] Choi J-H, Kim D-Y, Hockey BJ, Wiederhorn SM, Blendell JE, Handwerker CA. J Am Ceram Soc 2002;85:1841.
[60] Kitayama M, Glaeser AM. J Am Ceram Soc 2005;88:3492.
[61] Lee WH, Vanloon KR, Petrova V, Woodhouse JB, Loxton CM, Masel RI. J Catal 1990;126:658.
[62] McLean M, Mykura H. Surf Sci 1966;5:466.
[63] Cabie M, Giorgio S, Henry CR, Axet MR, Philippot K, Chaudret B. J Phys Chem C 2010;114:2160.
[64] Nabarro FRN. Proc Royal Soc London A1940;175:0519.
[65] Eshelby JD. Proc Royal Soc London A1957;241:376.
[66] Eshelby JD. Proc Royal Soc London A1959;252:561.
[67] Lee JK, Barnett DM, Aaronson HI. Metall Trans A 1977;8:963.
[68] Nabarro FRN. Dislocations in Solids. New York: Elsevier North-Holland Publishing Co.; 1986.
[69] Johnson WC, Voorhees PW. Diffus Defect Data Pt B 1992;23-24:87.
[70] Voorhees PW, McFadden GB, Johnson WC. Acta Metall et Mater 1992;40:2979.
[71] Thompson ME, Su CS, Voorhees PW. Acta Metall et Mater 1994;42:2107.
[72] Morris JW. Philos Mag 2010;90:3.
[73] Dahmen U. Metall Mater Trans A 1994;25:1857.
[74] Cahn JW, Kalonji G. in Aaronson HI, Sekerka RF, Laughlin DE, Wayman CM (Eds.). Solid->Solid Phase Transformations. Warrendale, PA: TMS-AIME; 1982. p.3.
[75] Kalonji G, Cahn JW. J De Physique 1982;43:25.
[76] Santala MK, Radmilovic V, Giulian R, Ridgway MC, Glaeser AM, Gronsky R. Scripta Mater

2010;62:187.
[77] Farrow RFC, Harp GR, Marks RF, Rabedeau TA, Toney MF, Weller D, Parkin SSP. J Cryst Growth 1993;133:47.
[78] Hildner ML, Minvielle TJ, Wilson RJ. Surf Sci 1998;396:16.
[79] Herring C. J Appl Phys 1950;21:301.
[80] Velho LR, Bartlett RW. Metall Trans 1972;3:65.
[81] Bergner D, Schwarz K. as cited in Impurity diffusion in noble metals. Landolt-Börnstien Database, Vol. 3, 1978:136.
[82] Heuer AH. J Eur Ceram Soc 2008;28:1495.
[83] Gontier-Moya EG, Bernardini J, Moya F. Acta Mater 2001;49:637.
[84] Blakely JM, Mykura H. Acta Metall 1962;10:565.
[85] Freyer N, Bonzel HP. Surf Sci 1985;160:L501.
[86] Preuss E, Freyer N, Bonzel HP. Appl Phys A-Mater Sci Process 1986;41:137.
[87] Henrichsen RA, Li CY. J Am Ceram Soc 1976;59:65.
[88] Dörre E, Hübner H. Alumina: processing, properties, and application. Berlin: Springer-Verlag; 1984.
[89] Reddy KPR. Oxygen diffusion in close-packed oxides. Cleveland: Case Western Reserve University; 1979.
[90] Prot D, LeGall M, Lesage B, Huntz AM, Monty C. Philos Mag A 1996;73:935.
[91] Nakagawa T, Sakaguchi I, Shibata N, Matsunaga K, Mizoguchi T, Yamamoto T, Haneda H, Ikuhara Y. Acta Mater 2007;55:6627.
[92] Kitayama M, Narushima T, Carter WC, Cannon RM, Glaeser AM. J Am Ceram Soc 2000;83:2561.
[93] Burton WK, Cabrera N, Frank FC. Philos Trans Royal Soc London A 1951;243:299.
[94] Metois JJ, Heyraud JC. J Cryst Growth 1982;57:487.
[95] Mullins WW, Rohrer GS. J Am Ceram Soc 2000;83:214.
[96] Rohrer GS, Rohrer CL, Mullins WW. J Am Ceram Soc 2001;84:2099.
[97] Cahn JW, Handwerker CA. Mater Sci Eng A 1993;162:83.
[98] Ziegler JF. SRIM/TRIM. http://www.srim.org/, 2003.
[99] White CW, Withrow SP, Sorge KD, Meldrum A, Budai JD, Thompson JR, Boatner LA. J Appl Phys 2003;93:5656.
[100] Collard SM, McLellan RB. Acta Metall Mater 1992;40:699.

6. Tables

Surface	Relative γ Reference [51]	Relative γ References [50, 52]
c$(0001)_\alpha$	1.00	1.00
r$\{10\bar{1}2\}_\alpha$	1.05 ± 0.04	0.855 ± 0.017
s$\{10\bar{1}1\}_\alpha$	1.07 ± 0.06	0.947 ± 0.016
a$\{1\bar{2}10\}_\alpha$	1.12 ± 0.07	0.974 ± 0.026
p$\{1\bar{2}13\}_\alpha$	1.06 ± 0.05	0.957 ± 0.026
m$\{10\bar{1}0\}_\alpha$	>1.16	>1.008
$\gamma_{max}/\gamma_{min}$	1.16	1.18

Table 1: Experimentally determined relative surface energies of undoped sapphire at 1600°C. The uncertainty represents the standard deviation.

Zone axis	Normalized measurement	Normalized dimension	Number of precipitates	Number of measurements	Standard deviation
$[0001]_\alpha$	$\frac{w_{\mathbf{a}(11\bar{2}0)_\alpha}}{w_{\mathbf{a}(1\bar{2}10)_\alpha}}$	1.00	14	42	0.01
	$\frac{w_{\mathbf{m}\{10\bar{1}0\}_\alpha}}{w_{\mathbf{a}(1\bar{2}10)_\alpha}}$	1.02	14	42	0.01
$[10\bar{1}0]_\alpha$	$\frac{w_{\mathbf{c}(0001)_\alpha}}{w_{\mathbf{a}(1\bar{2}10)_\alpha}}$	0.88	18	18	0.11
	$\frac{w_{\mathbf{p}\{1\bar{2}13\}_\alpha}}{w_{\mathbf{a}(1\bar{2}10)_\alpha}}$	0.99	18	34	0.03
	$\frac{w_{\{1\bar{2}16\}_\alpha}}{w_{\mathbf{a}(1\bar{2}10)_\alpha}}$	0.99	18	30	0.05
$[1\bar{2}10]_\alpha$	$\frac{w_{\mathbf{c}(0001)_\alpha}}{w_{\mathbf{m}(10\bar{1}0)_\alpha}}$	0.86	15	15	0.10
	$\frac{w_{\mathbf{r}(10\bar{1}\bar{2})_\alpha}}{w_{\mathbf{m}(10\bar{1}0)_\alpha}}$	0.98	15	20	0.03
	$\frac{w_{\mathbf{s}(10\bar{1}1)_\alpha}}{w_{\mathbf{m}(10\bar{1}0)_\alpha}}$	0.98	15	17	0.03
	$\frac{w_{\{10\bar{1}4\}_\alpha}}{w_{\mathbf{m}(10\bar{1}0)_\alpha}}$	0.98	15	18	0.05
	$\frac{w_{\{10\bar{1}\bar{5}\}_\alpha}}{w_{\mathbf{m}(10\bar{1}0)_\alpha}}$	0.95	15	10	0.05

Table 2: Normalized precipitate dimensions, $w_{(h_i k_i i_i l_i)_\alpha} / w_{(h_j k_j i_j l_j)_\alpha}$ for precipitates with the orientation relationship $(0001)_\alpha || (111)_{Pt}$; $[10\bar{1}0]_a || [1\bar{1}0]_{Pt}$.

Precipitate dimension normalized by $w_{\mathbf{a}(1\bar{2}10)_\alpha}$	Normalized dimension	Standard deviation
$w_{\mathbf{a}\{1\bar{2}10\}_\alpha}$	1.00	0.01
$w_{\mathbf{m}\{10\bar{1}0\}_\alpha}$	1.02	0.01
$w_{\mathbf{c}(0001)_\alpha}$	0.88	0.11
$w_{\mathbf{p}\{1\bar{2}13\}_\alpha}$	0.99	0.03
$w_{\{1\bar{2}16\}_\alpha}$	0.99	0.05
$w_{\mathbf{r}(10\bar{1}\bar{2})_\alpha}$	0.98	0.03
$w_{\mathbf{s}\{10\bar{1}1\}_\alpha}$	0.98	0.03
$w_{\{10\bar{1}4\}_\alpha}$	0.98	0.05
$w_{\{10\bar{1}\bar{5}\}_\alpha}$	0.95	0.05

Table 3: Normalized dimensions for precipitates with the orientation relationship $(0001)_\alpha||(111)_{Pt}$; $[10\bar{1}0]_a||[1\bar{1}0]_{Pt}$. All dimensions are normalized by $w_{\mathbf{a}(1\bar{2}10)_\alpha}$.

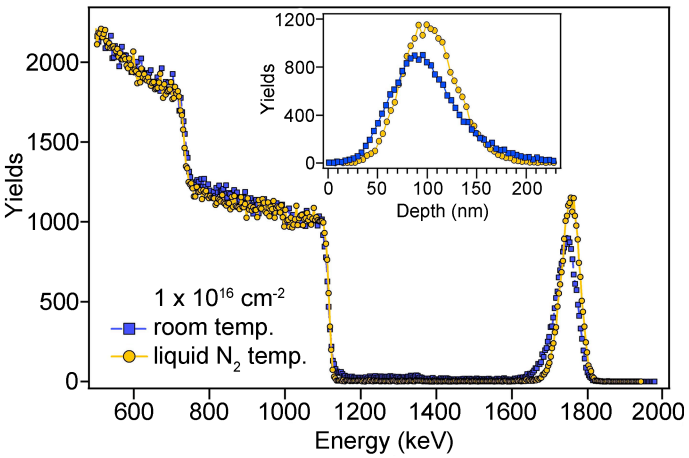

Figure 1 RBS spectra for sapphire substrates implanted at room temperature and with $l\!N_2$ cooling. The inset gives the Pt distribution as a function of distance from the sapphire surface.

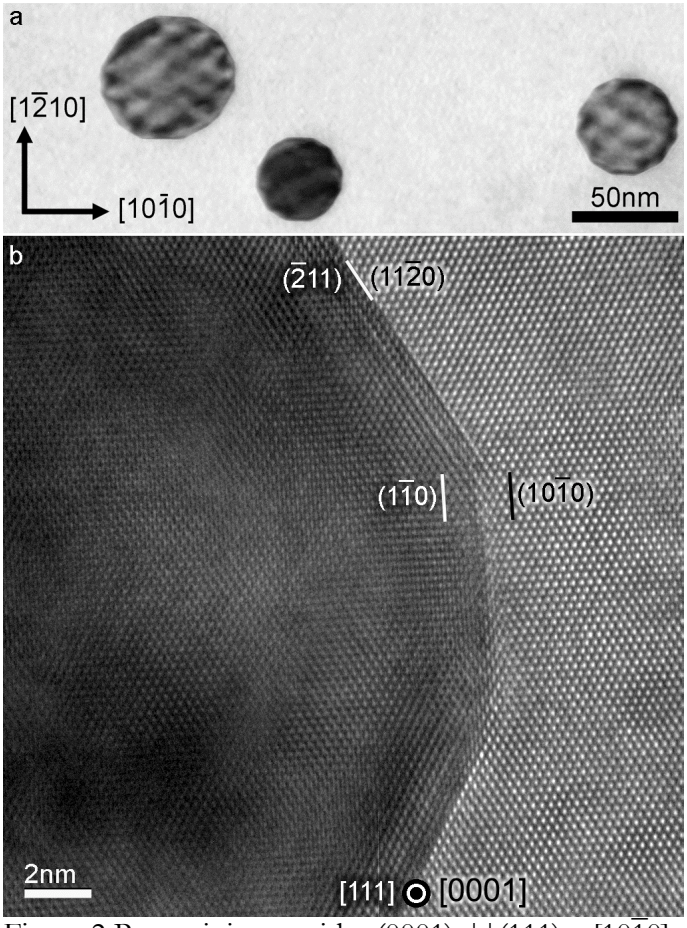

Figure 2 Pt precipitates with $\mathbf{c}(0001)_{\alpha}||(111)_{Pt}$; $[10\bar{1}0]_{\boldsymbol{\alpha}}||[1\bar{1}0]_{Pt}$ formed in sapphire after 100h at 1600°C, imaged with (a) bright-field TEM and (b) HRTEM.

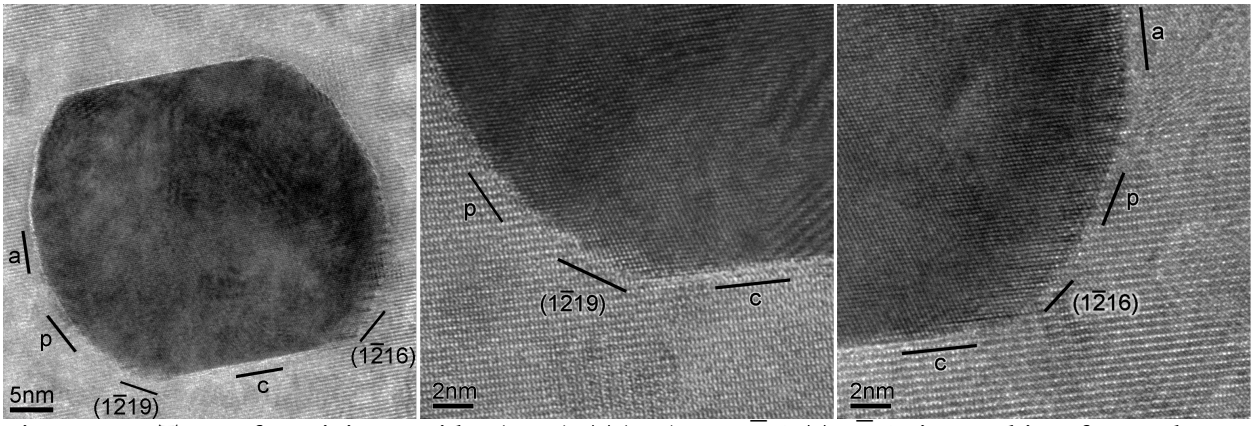

Figure 3 HRTEM of precipitates with $\mathbf{c}(0001)_\alpha||(111)_{Pt}$; $[10\bar{1}0]_\alpha||[1\bar{1}0]_{Pt}$ in sapphire after 100h at 1600°C viewed along the $[10\bar{1}0]_\alpha$ zone axis. Facets parallel to $[10\bar{1}0]_\alpha$ are labeled with respect to the sapphire.

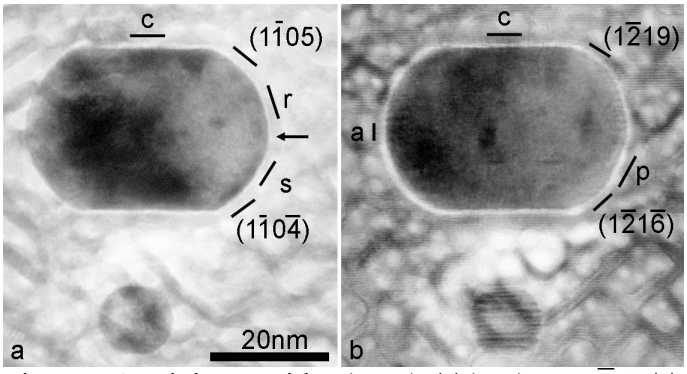

Figure 4 Precipitates with $\mathbf{c}(0001)_\alpha||(111)_{Pt}$; $[10\bar{1}0]_\alpha||[1\bar{1}0]_{Pt}$ viewed along the (a) $[1\bar{2}10]_\alpha$ and (b) $[10\bar{1}0]_\alpha$ zone axes. Facets parallel to the zone axes are labeled with respect to the sapphire. The arrow indicates part of an interface that is, in part, normal to $[10\bar{1}0]_\alpha$.

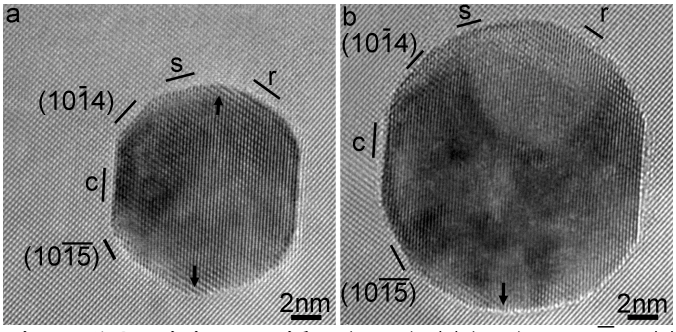

Figure 5 Precipitates with $\mathbf{c}(0001)_\alpha||(111)_{Pt}$; $[10\bar{1}0]_\alpha||[1\bar{1}0]_{Pt}$. Facets parallel to the $[1\bar{2}10]_\alpha$ zone axis are labeled. Arrows indicate portions of interfaces that are, in part, normal to $[10\bar{1}0]_\alpha$.

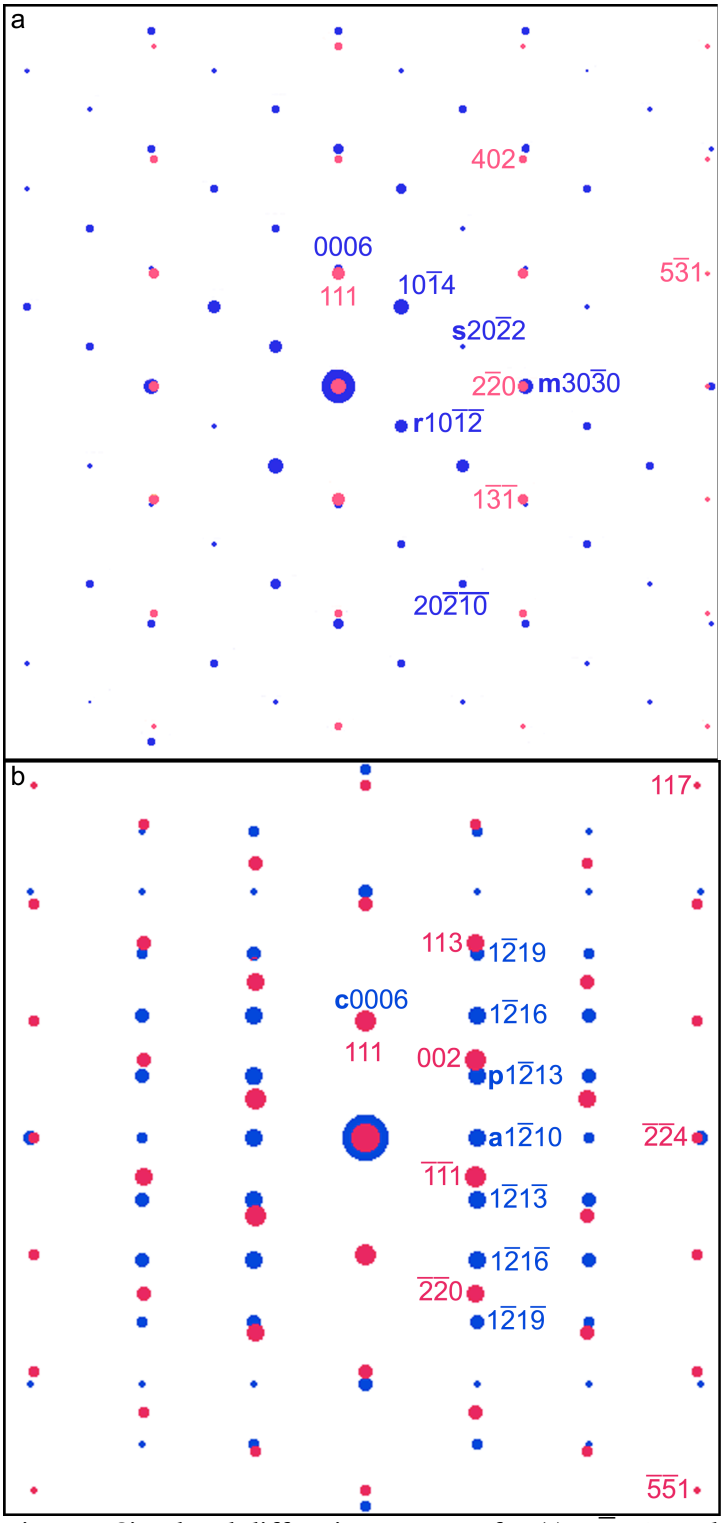

Figure 6 Simulated diffraction patterns for (a) $[1\bar{2}10]_{\alpha}$ and (b) $[10\bar{1}0]_{\alpha}$ zone axes.

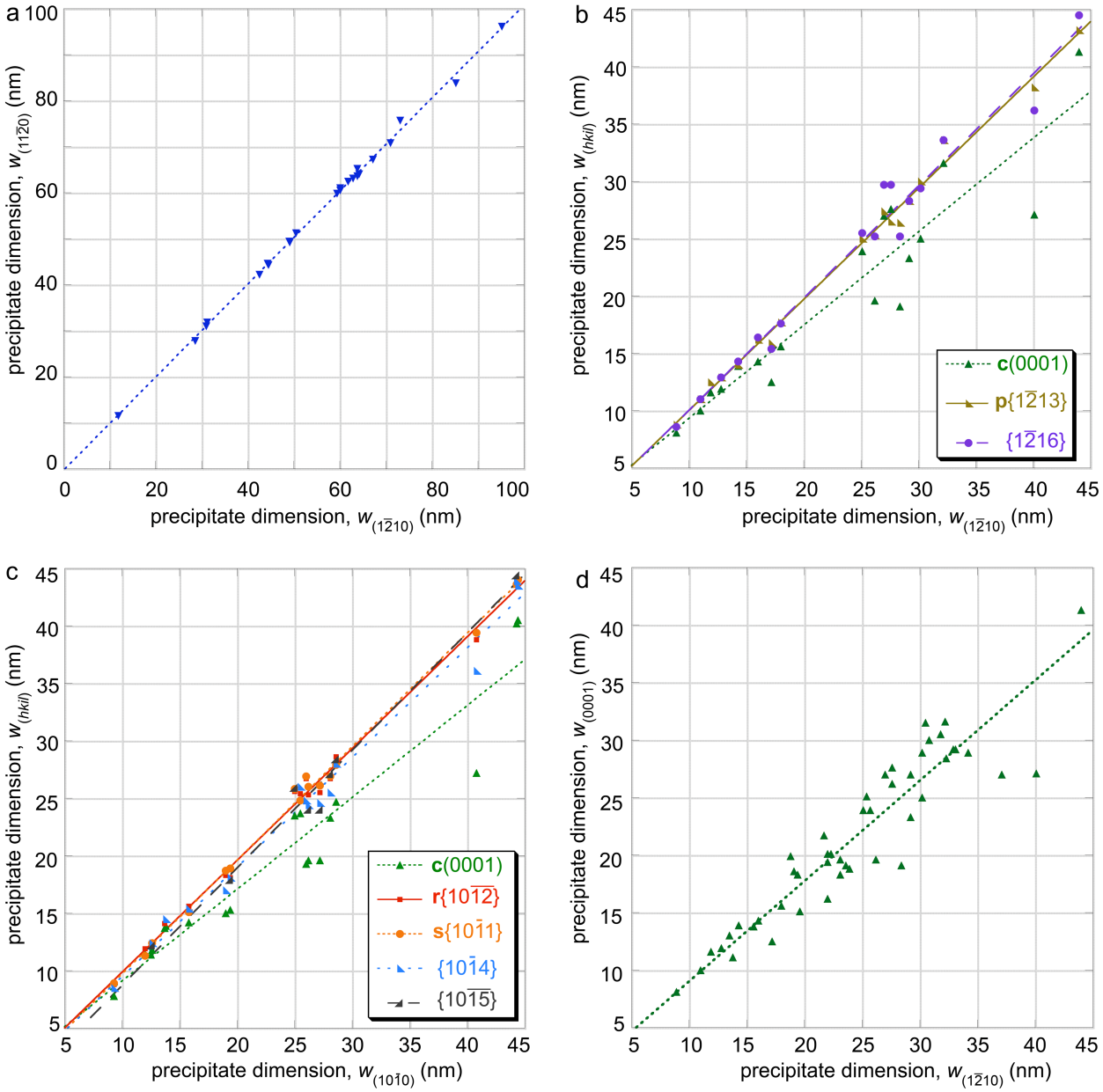

Figure 7 Plot of dimensions, $w_{(hkil)_\alpha}$, for precipitates with $(0001)_\alpha||(111)_{Pt}$; $[10\bar{1}0]_{\boldsymbol{\alpha}}||[1\bar{1}0]_{\mathbf{Pt}}$ when viewed along the (a) [0001], (b) $[10\bar{1}0]_{\boldsymbol{\alpha}}$, and (c) $[1\bar{2}10]_{\boldsymbol{\alpha}}$ zone axes, and (d) for just $w_{\mathbf{c}(0001)_\alpha}$ versus $w_{\mathbf{a}(1\bar{2}10)_\alpha}$. The lines are linear fits to the data. The error in $w_{(hkil)_\alpha}$ measurements is <0.5nm, approximately the size of the data markers.

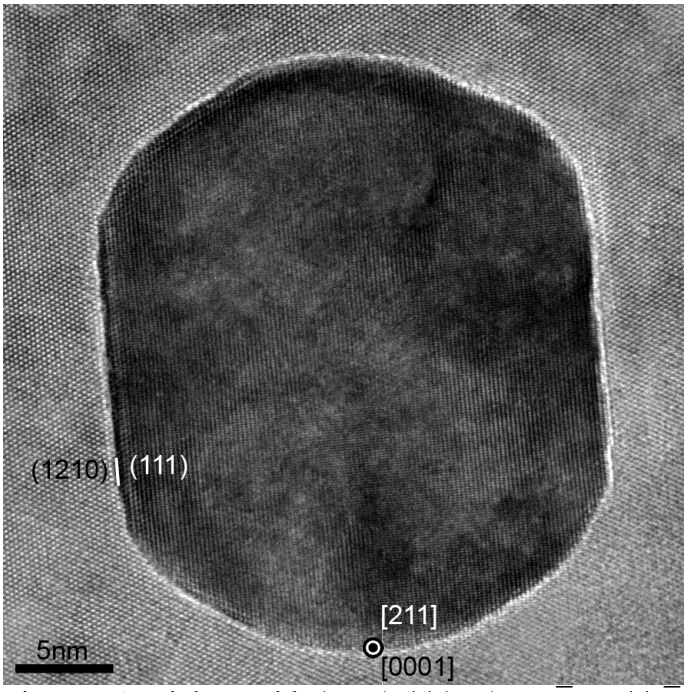

Figure 8 Precipitate with $(0001)_{\alpha}||(211)_{Pt}$; $[1\bar{2}10]_{\boldsymbol{\alpha}}||[\bar{1}11]_{\mathbf{Pt}}$ viewed along the $[0001]_{\alpha}$ zone axis after 100h at 1600°C; the morphology is distinct from precipitates with $(0001)_{\alpha}||(111)_{Pt}$; $[10\bar{1}0]_{\boldsymbol{\alpha}}||[1\bar{1}0]_{\mathbf{Pt}}$ when viewed along the same zone axis, c.f. Figure 2a.